PAPER • OPEN ACCESS

Investigation of slurry erosion-corrosion behavior of Ta(Si$_{1-x}$Al$_x$)$_2$ nanocrystalline coatings

View the article online for updates and enhancements.

Materials Research Express

PAPER

Investigation of slurry erosion-corrosion behavior of Ta(Si$_{1-x}$Al$_x$)$_2$ nanocrystalline coatings

Jiang Xu[1] [iD] , Qingwen Xie[1], Shuang Peng[1], Zhengyang Li[2] and Shuyun Jiang[3]

[1] Department of Material Science and Engineering, Nanjing University of Aeronautics and Astronautics, 29 Yudao Street, Nanjing 210016, People's Republic of China
[2] Institute of Mechanics, Chinese Academy of Sciences, Beijing 100190, People's Republic of China
[3] Department of Mechanical Engineering, Southeast University, 2 Si Pai Lou, Nanjing 210096, People's Republic of China

E-mail: xujiang73@nuaa.edu.cn

Abstract

To enhance the erosion-corrosion resistance of titanium alloys, two Ta(Si$_{1-x}$Al$_x$)$_2$ coatings with different Al content were deposited on Ti−6Al−4V alloy by double cathode glow discharge method. The coatings consist of single hexagonal C40 structured TaSi$_2$ phase, which forms an equiaxed grain structure with an average diameter of ∼5 nm. Al addition was found to enhance the values of H/E and adhesive strength between the substrate and coating. The erosion–corrosion behavior of the coatings was studied in a liquid–solid acid slurry flow (specifically a medium of 5 wt% HCl solution that contained a 10 wt% concentration of silica-based sand) using electrochemical measurements, weight loss tests and SEM observation. The results indicated that the ternary Ta(Si$_{0.875}$Al$_{0.125}$)$_2$ coating provided better protection, compared to the binary TaSi$_2$ coating, against the combined attack of mechanical erosion and electrochemical corrosion in a liquid–solid acid slurry flow. This is attributable to high self-healing ability of the surface passive film and a higher H/E ratio.

1. Introduction

As one of the most frequent material deterioration phenomena, erosion-corrosion damage is often found in many industrial operations involved in fluid handling, such pipelines, power plants, hydraulic turbines, marine and off-shore equipment etc [1, 2]. Under these conditions, industrial components often suffer from the joint action of mechanical erosion and electrochemical corrosion processes, through the action of solid erodent particles entrained in a corrosive fluid [3]. The slurry erosion-corrosion phenomenon, caused by the impact of a multi-phase flow medium, is primarily concerned with material surface characteristics, the erosion effect from solid particles (particles concentration, shape, size, hardness, etc) and the nature of the slurry medium itself. The complex interaction between the corrosion and erosion processes significantly accentuates material loss rates, which is dramatically greater than the simple sum of material removal rates caused by either pure mechanical erosion or static corrosion acting separately [4].

Over the past few decades, a number studies have devoted considerable effort to developing a fundamental understanding of the synergy between erosion and corrosion and its effect on materials degradation, through quantifying the synergistic components wear-enhanced-corrosion and corrosion-enhanced-wear, made possible by numerical simulation and experimental evaluation [5, 6]. As far as the slurry flow environment is concerned, the flow velocity plays an important role in the impact of erosion and corrosion on the material integrity, since it determines the frequency and energy of impacts exerted by solid particles suspended in a slurry medium [7]. From the viewpoint of material characteristics, the erosion-corrosion resistance of a material is not only intrinsically linked to its mechanical properties, such as hardness and toughness (represented by the capacity to absorb impact energy), but also closely tied to its electrochemical responses [8]. Therefore, it is essential to consider all these relevant factors in the design of high performance erosion-corrosion resistant material suitable for harsh environment.

Owing to their attractive properties including excellent corrosion resistance, biocompatibility and superior mechanical properties, titanium alloys have attracted increased application in industrial areas beyond military or commercial aerospace, for example, in marine and off-shore components [9]. However, they suffer low surface hardness and poor wear resistance, which limits the scope of their applications. Further, good corrosion resistance for titanium alloys is provided by the presence of a naturally formed and strongly adherent TiO_2 surface film. Nonetheless, the passive films formed on titanium alloys undergo severe rupture under aggressive environments, where strong acid, solid particles and high fluid speed act simultaneously on the surface of a component. This leads to the exposure of underlying fresh, bare substrates to the corrosive medium, due to damage of the passive film, which thus accelerates the metal dissolution process [10]. Since the corrosion, abrasion and erosion–corrosion resistance of a metallic material are strongly influenced by its surface properties rather than by its bulk properties, surface modification approaches are envisaged to be an effective strategy to reduce these limitations.

Transition metal silicides (TMS's) exhibit a range of excellent physical properties, including excellent high temperature oxidation resistance, a relatively high strength to weight ratio, high melting points and good creep resistance. This suggests these materials can be envisaged as candidate materials for applications at high temperature [11]. Of these compounds, $TaSi_2$, exhibits excellent potential for application as a wear-corrosion resistant thin film coating, because of its combination of high strength and hardness and effective resistance to corrosion [12]. However, as with many other transition metal disilicides, the very limited room temperature toughness of this compound limits its broader application. Alloying with silicides has been demonstrated to be an effective strategy to improve toughness [11]. It has been shown in our previous work that Al alloyed into a β-Ta_5Si_3 coating endowed a higher resistance to erosion-corrosion compared with the binary β-Ta_5Si_3 compound and uncoated 316 L stainless steel under two phase slurry flow (e.g. a 3.5 wt% NaCl solution that contains a 12 wt% concentration of silica sand) [13]. Hence, it is suggested that substitutional alloying with $TaSi_2$ may also provide tailored corrosion resistance along with mechanical properties to combat the synergistic actions of both corrosion and erosion. To our best knowledge, there were no reports available in the literature with regard to the erosion-corrosion behavior of $TaSi_2$ either as a bulk or coating material.

In the present work, a double cathode glow discharge method was used to prepare binary $TaSi_2$ and ternary Al containing $TaSi_2$ coatings onto Ti−6Al−4V substrates. Following the microstructural observation and mechanical properties measurements, erosion–corrosion tests were carried out on self-made apparatus under a liquid–solid acid slurry flow at different at flow velocities. The present study aims at clarifying the influence of incorporated Al on the erosion–corrosion resistance of the $TaSi_2$ coating.

2. Materials and methods

2.1. Coatings preparation
Substrate specimen with dimensions of 20 mm × 10 mm × 3 mm was cut from Ti−6Al−4V rods of chemical composition (in wt%): 6.04% Al, 4.03% V, 0.3% Fe, 0.1% O, 0.1%C, 0.05% N, 0.015% H, and Ti-balance. Firstly, the substrate specimen was ground by standard metallographic techniques with different grades of abrasive papers to obtain surface roughness of Ra $\sim$ 0.5 μm. Subsequently, the polished substrate specimen was ultrasonically cleaned in in acetone, alcohol, and finally dried with cold air. The binary $TaSi_2$ and ternary Al containing $TaSi_2$ coatings were deposited by a double cathode glow discharge system employing two targets with different stoichiometric ratios ($Ta_{20}Si_{80}$ and $Ta_{20}Si_{70}Al_{10}$), respectively. Before sputter deposition, the chamber was pumped down to a residual gas pressure of 5 × 10^{-4} Pa. Substrate specimen were etched by Ar ion bombardment at a potential of −650 V for 20 min to sweep any contamination from the of the specimen surface. The detailed deposition parameters used were as follows: the Ar gas pressure in the chamber maintaining at 35 Pa with an gas flow rate of 80 sccm, substrate bias voltage (−300 V) with impulse current (a pulse frequency and a duty circle set at 1100 Hz and 85%, respectively); target electrode bias voltage (−900 V) with direct current (3.1 × 10^{-2} A cm^{-2}); distance between targets and substrate of 10 mm; a deposition temperature setting at 800 °C and a processing time of 3 h.

2.2. Coating characterization
The phase analysis of the as-received coatings was examined by x-ray diffractometer (XRD, D8 ADVANCE, Cu-Kα irradiation, 30 mA, 40 kV). The diffraction spectra of the coatings were recorded with a scanning 2θ angle range from 20° to 80° at a scanning speed of 3 °min^{-1}. The surface and cross-sectional morphologies of the as-deposited coatings were examined by FE-SEM (Hitachi, S-4800, Japan), equipped with an energy dispersive spectrometer (EDS) attachment (EDX-4;Philips). A JEOL JEM-2010 transmission electron microscope (TEM) was employed to observe of both plan-view and cross-sectional microstructure of the coatings operated at an accelerating voltage of 200 kV. Plan-view TEM sample preparation was fabricated by mechanically thinning

from the backside of the coated sample and then thinned to electron transparency using a single-jet electrochemical polishing method. Cross-sectional TEM specimens were accomplished by a focused ion beam (FIB) microscope (FEI xP200, FEI Company, Hillsboro, OR).

Hardness and elastic modulus of the as-deposited coatings were measured with a Berkovich diamond indenter using a UMIS workstation (Ultra-Micro Indentation System 2000). The measurements were performed with a maximum load of 20 mN and a loading rate of 20 mN min^{-1}. Hardness and the elastic modulus were determined by the Oliver-Pharr method [14] obtained from the measured load-depth curves. The tests were performed ten times for each specimen and its average value of 10 indentations was calculated to obtain reliable data. A commercial CSM Revetest scratch tester was used to evaluate the adhesive strength between the coating and the Ti−6Al−4V substrate. During scratching test, a diamond stylus with 0.2 mm of a tip radius of (120° cone angle) was drawn across the coating surface by continuously increasing the normal load at a loading rate of 100 N min^{-1} and a scratch velocity of 10 mm min^{-1}. The friction coefficient, friction force and penetration depth were simultaneously recorded and presented as a function of the displacement of the diamond stylus. The adhesion strength of the coatings can be determined by the signal of penetration depth and friction force, as well as the observation of scratch tracks morphologies.

2.3. Erosion-corrosion tests and electrochemical measurements

Erosion–corrosion characteristics of samples were assessed using a self-made device, which has been described elsewhere [15]. The acid slurry was composed of 5 wt% HCl solution and 10 wt % SiO$_2$ sand particles and the average particle size of sand particles is about 200 μm. During the erosion–corrosion test, the samples mounted at the sample holder rotated at different given rotation velocities (2.50, 3.13, 3.76 and 4.39 m s^{-1}) along the central axis. It should be noted that the rotation speeds of a sample determines the flow velocity of acid slurry. The weight loss of the samples was measured with an analytical electronic microbalance of an accuracy of 0.01 mg before and after each subsequent erosion-corrosion test interval. Each test was repeated at least three times under identical conditions to ensure the reproducibility. Under liquid–solid acid slurry flow conditions, the total weight loss (W_t) can be split into three components: pure corrosion (W_c), pure erosion (W_e) and synergistic components between erosion and corrosion (W_{ec}). In this work, the pure erosion component (W_e) is determined by measuring the weight loss tested in distilled water containing 10 wt % concentration of SiO$_2$ sand particles; the pure corrosion component (W_c) is determined by measuring the weight loss tested in 5 wt% HCl solution without the addition of silica sand particles; the synergistic components (W_{ec}) can be calculated from the weight difference between W_t and the sum of W_e and W_c.

Electrochemical measurements were used to monitor the changes in corrosion characteristics of the samples under acid slurry flow conditions. Electrochemical tests were conducted with a CHI 660 C electrochemical workstation (Shanghai ChenHua Instruments Inc., China) using a saturated calomel reference electrode (SCE) and platinum plate as a counter electrode. All the potentials described in the paper were relative to the SCE. During the current response and open circuit potential (OCP) measurements, the variations of the rotational velocities of a sample as a function of exposure time are presented in figure 1. Current response tests were performed at a constant potential of +0.6 V$_{SCE}$. Potentiodynamic polarization experiments were conducted at a potential sweep rate of 1 mV s^{-1} from −0.5 to +1.5 V$_{SCE}$. The electrochemical impedance spectroscopy (EIS) tests were carried out at an open circuit potential (OCP) using a perturbation amplitude of 10 mV over a range of frequencies from 100 kHz to 10 mHz.

3. Results and discussion

3.1. Phase composition and microstructure of Ta(Si$_{1−x}$Al$_x$)$_2$ coatings

Figure 2 shows typical x-ray diffraction (XRD) patterns obtained from both binary TaSi$_2$ and ternary Al containing TaSi$_2$ coatings, along with the powder diffraction file data (JCPDS Card No. 38–0483) of hexagonal C40 structured TaSi$_2$ (marked by vertical black lines). It can be seen from figure 2 that the two as-received Ta(Si$_{1−x}$Al$_x$)$_2$ coatings have similar patterns where all characteristic diffraction peaks are well matched with that of hexagonal C40 structured TaSi$_2$. Compared with the binary TaSi$_2$ coating, all the diffraction peaks for the Ta(Si$_{0.875}$Al$_{0.125}$)$_2$ coating move towards lower 2θ angles slightly, which is consequent on the incorporation of Al in the TaSi$_2$ lattice. Since the atomic radius of Al is larger than that of Si, Al alloying results in an expanded lattice of crystal TaSi$_2$. In addition, both the two XRD patterns display broad and low-intensity diffraction lines, indicating that the two as-received coatings possess very fine grain.

Figure 3 shows SEM images and EDX elemental maps of the cross-section of the two as-received Ta(Si$_{1−x}$Al$_x$)$_2$ coatings deposited onto the Ti−6Al−4V substrates, together with the results of EDS spectra of the selected area in the coatings. The cross-sectional SEM images of both binary TaSi$_2$ (figure 3(a)) and ternary Al containing TaSi$_2$ coatings (figure 3(d)) display three distinct regions with a marked contrast difference, namely, a
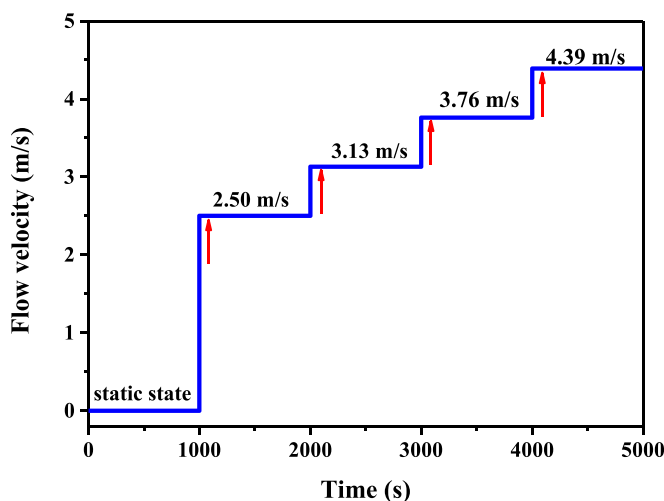
Figure 1. The flow velocities of the tested samples as a function of exposure time curve.
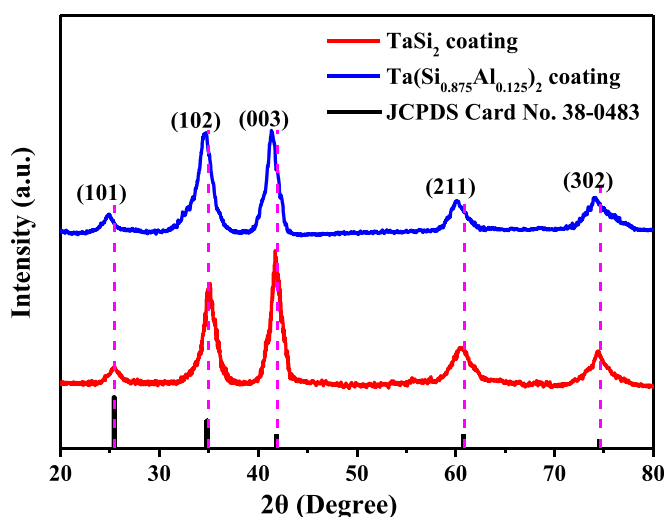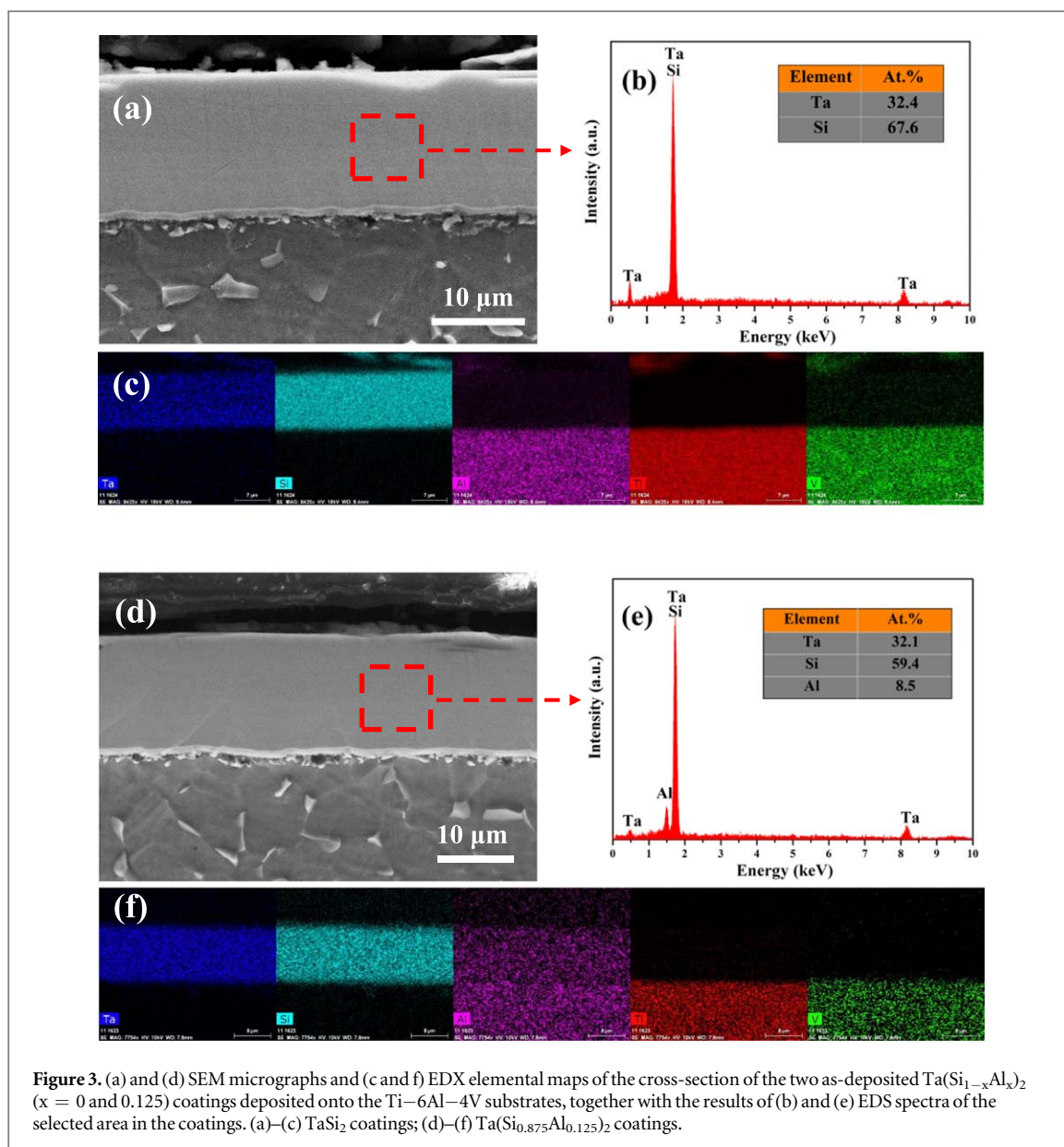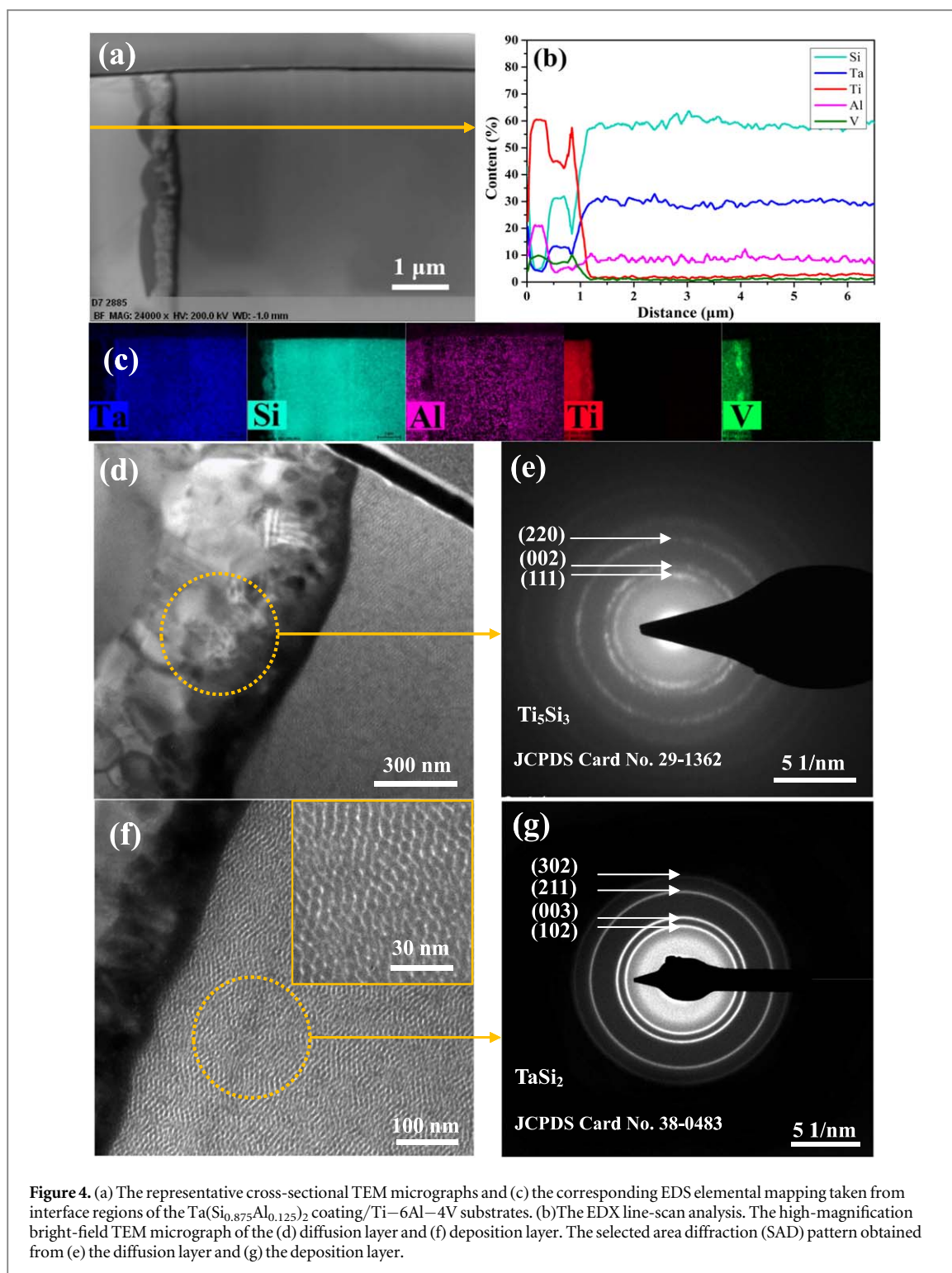

Figure 2. The XRD patterns of the $TaSi_2$ and the Al-containing $TaSi_2$ coatings.

$Ta(Si_{1-x}Al_x)_2$ deposition layer, a thin diffusion layer and underlying Ti−6Al−4V substrate from the top to the bottom, respectively. Unlike other thin film deposition techniques, the higher deposition temperature used here, promotes diffusion of deposition atoms towards substrate to generate interfacial diffusion layer, because the diffusion of those atoms is strongly dependent on deposition temperature. From the cross-sectional morphologies shown in figure 3, the dense and homogenous $Ta(Si_{1-x}Al_x)_2$ coatings with a thickness of ∼15 μm are tightly adhered to Ti−6Al−4V substrate, and no evidence of micro-cracks or defects exists at both inside of the $Ta(Si_{1-x}Al_x)_2$ deposition layers and interfacial region of the coating/substrate, which brings tremendous benefit to mechanical properties of the coatings. As can be seen from the EDS elemental maps ((figures 3(c) and (f)), Ta, Si and Al elements are uniformly distributed across the entire coating. EDS analysis of the selected area ((figures 3(b) and (e)) further reveals that the element composition percentages of the binary and ternary coatings are $Ta_{32.4}Si_{67.6}$ and $Ta_{32.1}Si_{59.4}Al_{8.5}$ (in at.%), and their stoichiometry are close to $TaSi_2$ and $Ta(Si_{0.875}Al_{0.125})_2$.

To gain insight into the microstructural characteristics of $Ta(Si_{1-x}Al_x)_2$ coatings and the coating/substrate interface, both cross-sectional and plan-view TEM images of the $Ta(Si_{0.875}Al_{0.125})_2$ coating were acquired. Figure 4 presents the representative cross-sectional TEM micrographs and the corresponding EDS elemental mapping taken from interface regions of the $Ta(Si_{0.875}Al_{0.125})_2$ coating/Ti−6Al−4V substrates. Similar to that seen in the cross-sectional SEM image, three distinct regions with a sharp interface are detectable in figure 4(a): a coarse grained Ti−6Al−4V substrate on top which exists the fine grained intermediate diffusion layer ∼600 nm in thickness and then a uniform and compact $Ta(Si_{1-x}Al_x)_2$ deposition layer. High-magnification bright-field

Figure 3. (a) and (d) SEM micrographs and (c and f) EDX elemental maps of the cross-section of the two as-deposited $Ta(Si_{1-x}Al_x)_2$ (x = 0 and 0.125) coatings deposited onto the Ti−6Al−4V substrates, together with the results of (b) and (e) EDS spectra of the selected area in the coatings. (a)–(c) $TaSi_2$ coatings; (d)–(f) $Ta(Si_{0.875}Al_{0.125})_2$ coatings.

TEM micrograph (figure 4(d)) indicates that the intermediate diffusion layer consists of relatively coarse grains closer to the Ti−6Al−4V substrate and becomes gradually finer towards the $Ta(Si_{1-x}Al_x)_2$ deposition layer. EDX line-scan analysis (figure 4(b)) indicates that the intermediate diffusion layer is predominantly enriched in Ti and Si with only small amounts of Ta, Al and V, and Si /Ta atomic ratio is significantly higher than 2, denoting a preferred diffusion of Si from the $Ta(Si_{1-x}Al_x)_2$ deposition layer to the Ti−6Al−4V substrate. In the selected area diffraction (SAD) pattern (figure 4(e)) obtained from the diffusion layer, the main Miller indexes (hkl) of discrete diffraction rings are labelled and the interplanar spacings of the diffraction rings correspond exactly to those for hexagonal $D8_8$-structured Ti_5Si_3. Based on an empirical rule of ordered Cu_3Au [16], for a ordered A_xB_y compounds, if the ratio of x to y is bigger than 2, the diffusion of the majority element A should be much faster than that for the minority element B. Therefore, Si element is supposed to diffuse faster than Ta element in the $Ta(Si_{1-x}Al_x)_2$ deposition layer during the deposition process, and the growth of the Ti_5Si_3 is determined by reaction diffusion between Si atoms and the Ti–6Al–4 V substrate. Such diffusion layer might contribute to the better anchored of the $Ta(Si_{1-x}Al_x)_2$ deposition layer to the substrate. From the cross-sectional TEM view of the $Ta(Si_{1-x}Al_x)_2$ deposition layer (figure 4(f)), the deposition layer is typically equiaxed cellular structure, with a homogeneous distribution of grain size in the range of about 5 ∼ 7 nm. Diffraction reflections of (102), (003) and (211) for hexagonal C40 structured $TaSi_2$ can be clearly seen in the SAD patterns (figure 4(g)). It's important to note that the $Ta(Si_{1-x}Al_x)_2$ deposition layer exhibits a densified nanostructured and non-columnar microstructure, which is different from the microstructural feature of common PVD coatings [17, 18]. Since the PVD method is characteristic of directional surface deposition method, the resultant coatings exhibit a columnar-like growth, and a number of intrinsic defects, especially permeable defects, are widely present

Figure 4. (a) The representative cross-sectional TEM micrographs and (c) the corresponding EDS elemental mapping taken from interface regions of the Ta(Si$_{0.875}$Al$_{0.125}$)$_2$ coating/Ti−6Al−4V substrates. (b)The EDX line-scan analysis. The high-magnification bright-field TEM micrograph of the (d) diffusion layer and (f) deposition layer. The selected area diffraction (SAD) pattern obtained from (e) the diffusion layer and (g) the deposition layer.
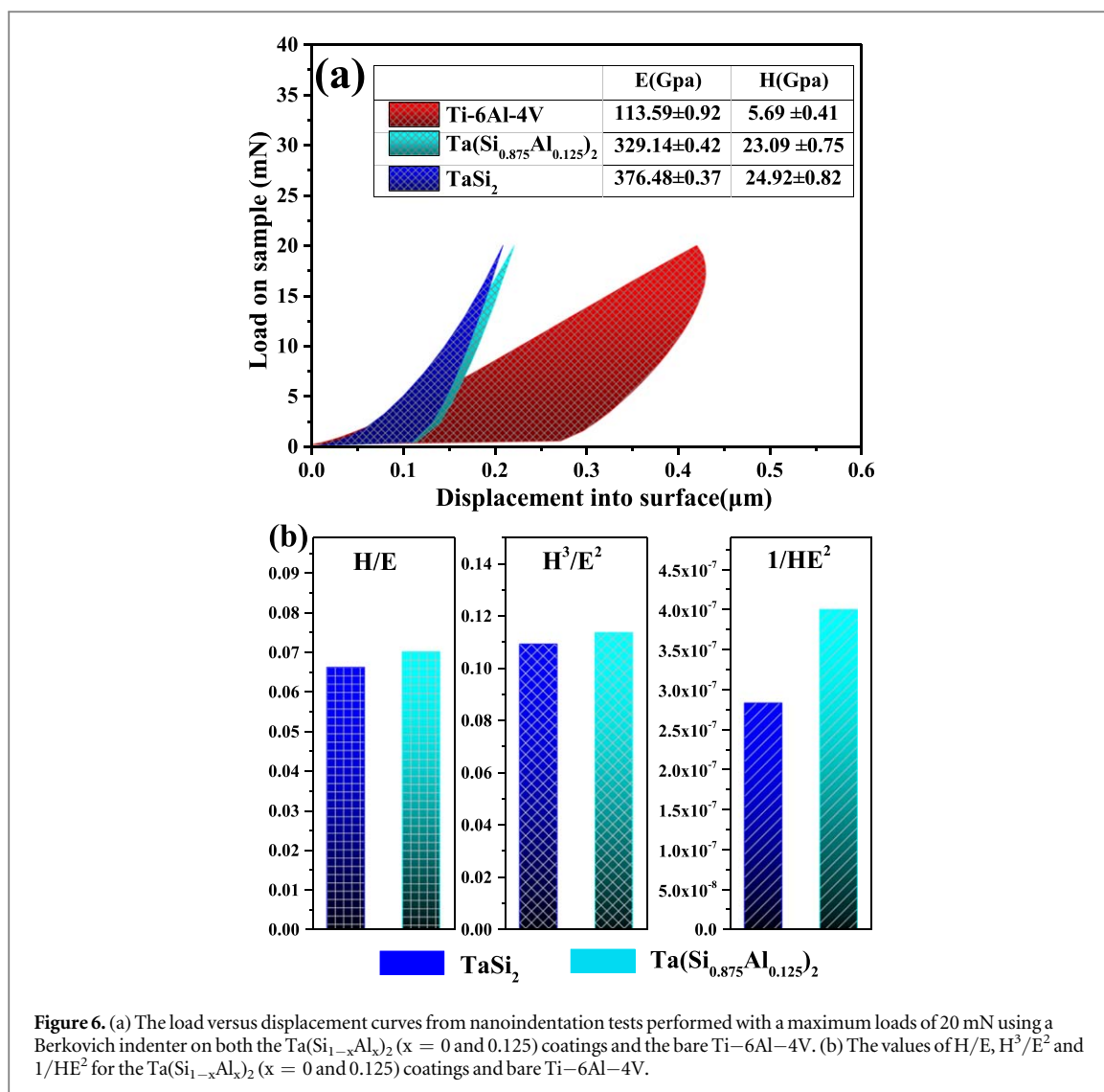
between these columnar grains. These defects, providing direct paths for the corrosive electrolyte penetrating to the substrate, would be undoubtedly harmful to the corrosion resistance of the coatings. From the microstructural point of view, the Ta(Si$_{1-x}$Al$_x$)$_2$ coatings with a dense and non-columnar microstructure are desirable to achieve excellent corrosion resistance. Figure 5 shows typical bright-field TEM and HRTEM micrographs of the Ta(Si$_{0.875}$Al$_{0.125}$)$_2$ deposition layer taken from a plan-view sample, along with a Fourier diffractogram presented as top left insert in figure 5(b). The Ta(Si$_{0.875}$Al$_{0.125}$)$_2$ deposition layer exhibits a dense nanocrystalline configuration and the equiaxed grains with an average size of ∼5 nm, as evidenced by the high-resolution TEM image (figure 5(b)). To enhance the image quality, Digital Micrograph software was employed to analyze the high-resolution TEM image, as shown on both the left and right sides in figure 5(b). Clearly, these equiaxed grains, highlighted by dotted white line, partially overlap with each other along the electron beam

Figure 5. (a) The typical bright-field plan-view TEM of the Ta(Si$_{0.875}$Al$_{0.125}$)$_2$ deposition layer. (b) The high-resolution TEM micrographs along with a Fourier diffractogram.
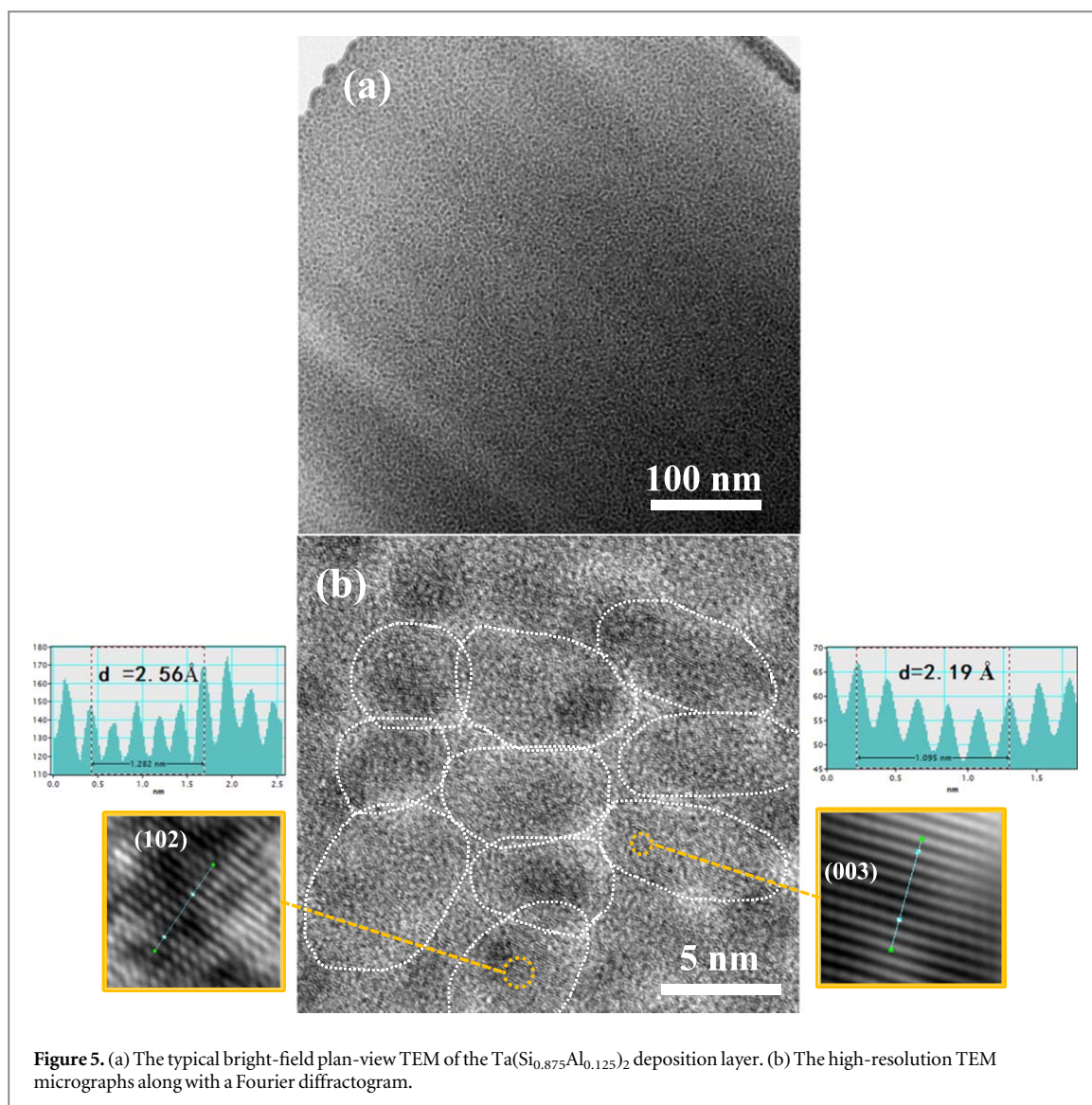
direction and the *d* spacings of line fringes were measured to be 2.56 Å and 2.19 Å, which are identified as the crystal planes of (102) and (003) for hexagonal C40 structured TaSi$_2$, respectively.

3.2. Mechanical properties

Figure 6 shows the normal load-displacement plots from nanoindentation tests performed with a maximum loads of 20 mN using a Berkovich indenter on the two Ta(Si$_{1-x}$Al$_x$)$_2$ coatings and bare Ti6Al4V alloy. Clearly, the maximum penetration depths and residual impression depths are much smaller for the two coatings as compared to bare Ti−6Al−4V, implying that plastic deformation resistance of bare Ti−6Al−4V is enhanced by coating with Ta(Si$_{1-x}$Al$_x$)$_2$. With more than 10 indentations, the average hardness values of the binary TaSi$_2$ and ternary Al containing TaSi$_2$ coatings are 24.92 ± 0.82 GPa and 23.09 ± 0.75 GPa, respectively, which are about 4.4 and 4.1 times, respectively, bigger than that of untreated Ti−6Al−4V (5.69 ± 0.41 GPa). Similarly, the values of the elastic modulus for the binary TaSi$_2$ and ternary Al containing TaSi$_2$ coatings are about 3.3 and 2.9 times higher than that of uncoated Ti−6Al−4V alloy (113.59 ± 0.92 GPa), respectively. And it is also worth noting that the values of hardness and elastic modulus for the binary TaSi$_2$ coating are much greater than those documented in the literature. For instance, the hardness of heated sintered TaSi$_2$, which is composed of many nanometer-sized grains (an average grain size about 60 nm), was measured to be 13 GPa [19]and the values of hardness and elastic modulus for a bent TaSi$_2$ fiber was observed to be 11 GPa and 251 GPa, respectively [20]. This phenomenon also has been found in other nanocrystalline metal silicides coatings reported in our previous works, which was is directly traceable to the nanoscale grain with an average grain size less than 10 nm and dense microstructure [21]. Moreover, the values of hardness and elastic modulus of the TaSi$_2$ coating are slightly reduced by the addition of Al, indicating that Al alloying leads to solid solution softening for TaSi$_2$. Usually, the higher hardness combined with the lower modulus signifies not only higher resistance to plastic deformation,

Figure 6. (a) The load versus displacement curves from nanoindentation tests performed with a maximum loads of 20 mN using a Berkovich indenter on both the $Ta(Si_{1-x}Al_x)_2$ (x = 0 and 0.125) coatings and the bare Ti−6Al−4V. (b) The values of H/E, H^3/E^2 and $1/HE^2$ for the $Ta(Si_{1-x}Al_x)_2$ (x = 0 and 0.125) coatings and bare Ti−6Al−4V.

but also allowing contact pressure to be distributed over a wider area. Several researches employed the H/E and H^3/E^2 ratios as mechanical indexes to evaluate the plastic deformation resistance and tribological performance of coatings [22–24]. They also found that the higher H/E (fracture toughness index) and H^3/E^2 (plastic deformation resistance) ratios, the greater fracture toughness and wear resistance of those coating. Furthermore, the parameter of $1/HE^2$ is proportional to the threshold load for crack initiation under abrasive wear condition and can be used as a key parameter to forecast the abrasion damage tolerance [25]. As shown in figure 6(b), Al alloying increases the values of H/E, H^3/E^2 and $1/HE^2$ for the $TaSi_2$ coating, denoting an improved the mechanical properties of the $TaSi_2$ coating through Al addition.

Owing to different deformation responses of the coating and the substrate on which it is deposited, insufficient adhesion of the coating to the substrate may lead to detachment of the coating by the formation of micro-cracks, inducing adhesive failure at a certain load. Hence, strong coating adhesion is essential for practical application. In the present study, nano-scratch tests were performed on the $Ta(Si_{1-x}Al_x)_2$ (x = 0 and 0.125) coatings to determine qualitatively the adhesion of the coatings to the Ti−6Al−4V substrates. During the scratch tests, the adhesion characteristics of the coatings are characterized by two critical loads (i.e. L_{c1} and L_{c2}), where L_{c1} and L_{c2} are defined as the minimum loads required to initiate scratch micro-cracks and to remove the coating completely, respectively [26, 27]. Commonly, L_{c1} is determined by careful examination of the scratch morphology, because the friction force curves are quite insensitive to local cracking events within the coating. Figure 7(a) shows typical tangential friction force and penetration depth as a function of normal force for the $Ta(Si_{1-x}Al_x)_2$ (x = 0 and 0.125) coatings. As observed from figure 7(a), at an early stage of the scratch test, the friction force and penetration depth rise slowly, and when the normal forces increase to 41 N and 48 N for the $TaSi_2$ and $Ta(Si_{0.875}Al_{0.125})_2$ coatings, respectively, a sharp increase in tangential friction force and an penetration depth are easily recognizable, indicating that the Lc_2 values have been reached for the coatings. To explore the coating failure mechanisms of the two coatings, the scratch track morphologies were observed by
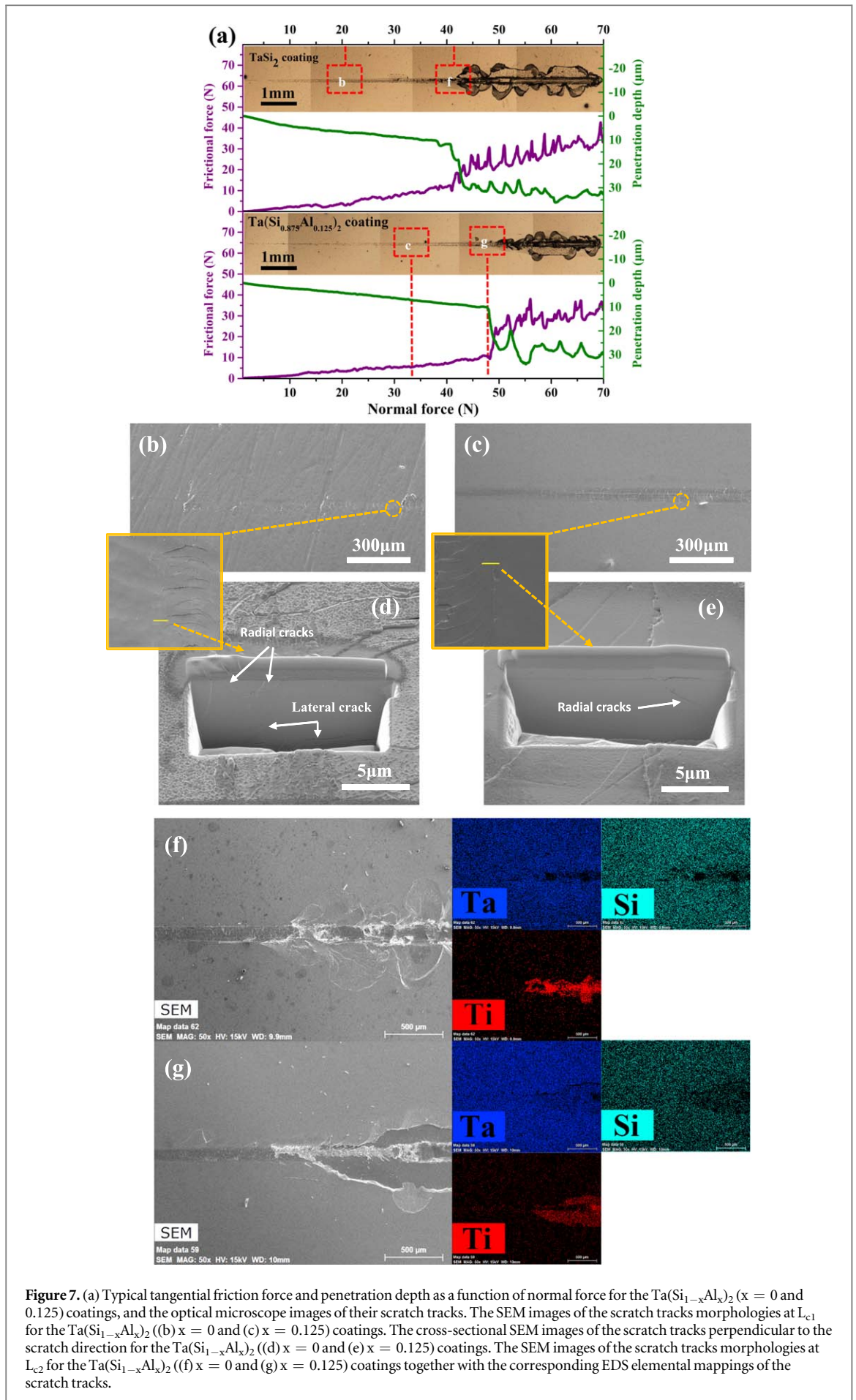
Figure 7. (a) Typical tangential friction force and penetration depth as a function of normal force for the Ta(Si$_{1-x}$Al$_x$)$_2$ (x = 0 and 0.125) coatings, and the optical microscope images of their scratch tracks. The SEM images of the scratch tracks morphologies at L$_{c1}$ for the Ta(Si$_{1-x}$Al$_x$)$_2$ ((b) x = 0 and (c) x = 0.125) coatings. The cross-sectional SEM images of the scratch tracks perpendicular to the scratch direction for the Ta(Si$_{1-x}$Al$_x$)$_2$ ((d) x = 0 and (e) x = 0.125) coatings. The SEM images of the scratch tracks morphologies at L$_{c2}$ for the Ta(Si$_{1-x}$Al$_x$)$_2$ ((f) x = 0 and (g) x = 0.125) coatings together with the corresponding EDS elemental mappings of the scratch tracks.
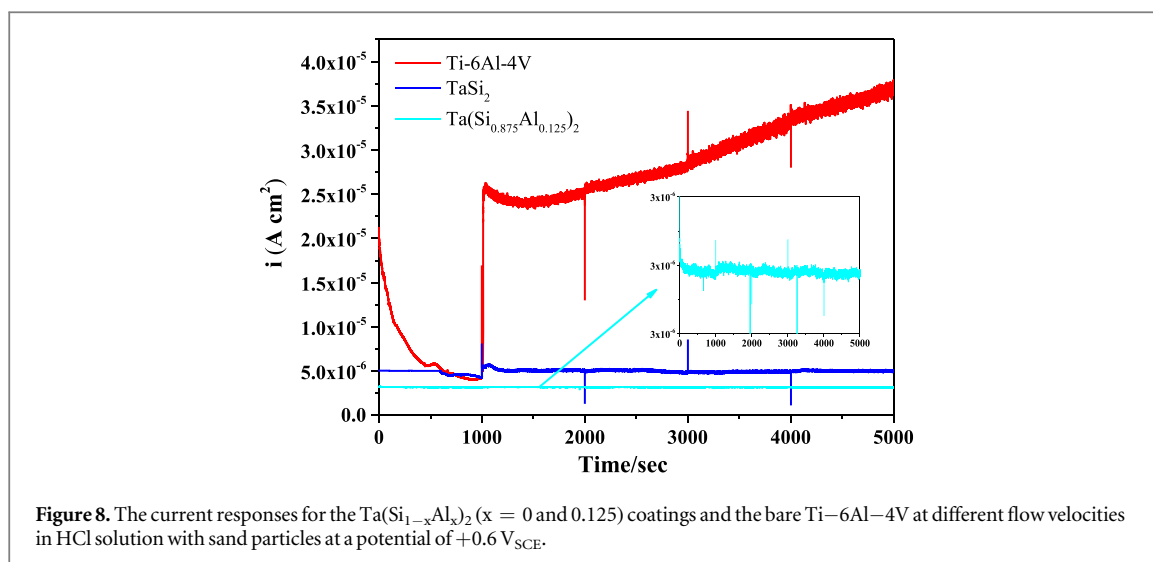
Figure 8. The current responses for the $Ta(Si_{1-x}Al_x)_2$ (x = 0 and 0.125) coatings and the bare Ti−6Al−4V at different flow velocities in HCl solution with sand particles at a potential of +0.6 V_{SCE}.

optical microscopy (OM) and SEM-EDS, as shown in figure 7(b∼g). In the initial stages of the scratch test, the scratch grooves are very smooth without appreciable damage. Subsequently, the width of scratch grooves and the degree of plastic deformation created by the sliding indenter increase as the normal load increased. When the normal load is increased to L_{c1} (21 N for the $TaSi_2$ coating and 33 N for the $Ta(Si_{0.875}Al_{0.125})_2$ coating), the tensile stresses developed at the rear of the sliding indenter are high enough to induce radial cracks, which are normal to the scratch direction. The cross-sectional secondary electron images of the scratch tracks, prepared perpendicular to the scratch direction, indicate that for the $Ta(Si_{0.875}Al_{0.125})_2$ coating, only radial cracks propagating downwards at an angle to the coating surface are observed. In contrast, for the $TaSi_2$ coating, some radial cracks run down and connect with lateral cracks, emanating from the coating/substrate interface, which then extend away toward the outside of the scratch track. With a further increase in the normal load, the density of the cracks increases, and chipping of the coating appears at the edges of the scratch tracks. When the critical load L_{c2} is reached for both coatings, the indenter has penetrated much of the coating thickness and the coatings exhibit continuous spallation so that the underlying substrate is exposed. EDS elemental mapping of the scratch tracks show that the center of the scratch groove yields a strong Ti signal, indicating complete removal of the coatings. It is evident that the $Ta(Si_{0.875}Al_{0.125})_2$ coating exhibits higher adhesion strength and greater crack initiation load than the $TaSi_2$ coating, denoting that Al additions enhance the load bearing capacity of the $TaSi_2$ coating.

3.3. Slurry erosion-corrosion properties

3.3.1. Current responses/Open circuit potential (OCP)

Figure 8 shows the evolution of current densities with rotational velocity for the $Ta(Si_{1-x}Al_x)_2$ (x = 0 and 0.125) coatings and bare substrate potentiostatically polarized at a potential of +0.6 V_{SCE} in a liquid–solid acid slurry flow (5 wt% HCl solution containing a 10 wt% concentration of silica sand). The applied potential of +0.6 V_{SCE} coincides with potential of the passive range in potentiodynamic polarization curves of the tested samples under both static and dynamic conditions, as will be subsequently described. For the uncoated substrate, under static condition, the current density decreases gradually with immersion time, which may be related to a passive film grown on the electrode surface and the current density needed to maintain the passivation is reduced with thickening of the passive film. As the Ti−6Al−4V sample begins to rotate, the current density increases rapidly and then shows a steady rise with an increase in rotational velocity step by step, accompanied by continuous oscillations in current density. For a passive material, the surface passive film plays an important role in counteracting the acid slurry impingement and its current response is determined primarily by the competition process between de-passivation and re-passivation. The rise in current density for bare Ti−6Al−4V originates from either local damage of the passive film or the thinning of passive film induced by impact from solid particles, that is, the de-passivation of the passive film predominates over re-passivation under dynamic conditions [28–30]. In contrast, there was no significant difference in the current density values for the two coatings, in particular for the $Ta(Si_{0.875}Al_{0.125})_2$ coating, under both static and dynamic conditions with only minimal fluctuations in value. Moreover, the current densities for both coatings were of the order of 10^{-6} A cm^{-2}, which is one order of magnitude lower than that for bare Ti−6Al−4V. Hence, compared with uncoated Ti−6Al−4V, the local breakdown of the passive films formed on the two coatings is significantly suppressed during slurry erosion corrosion tests.
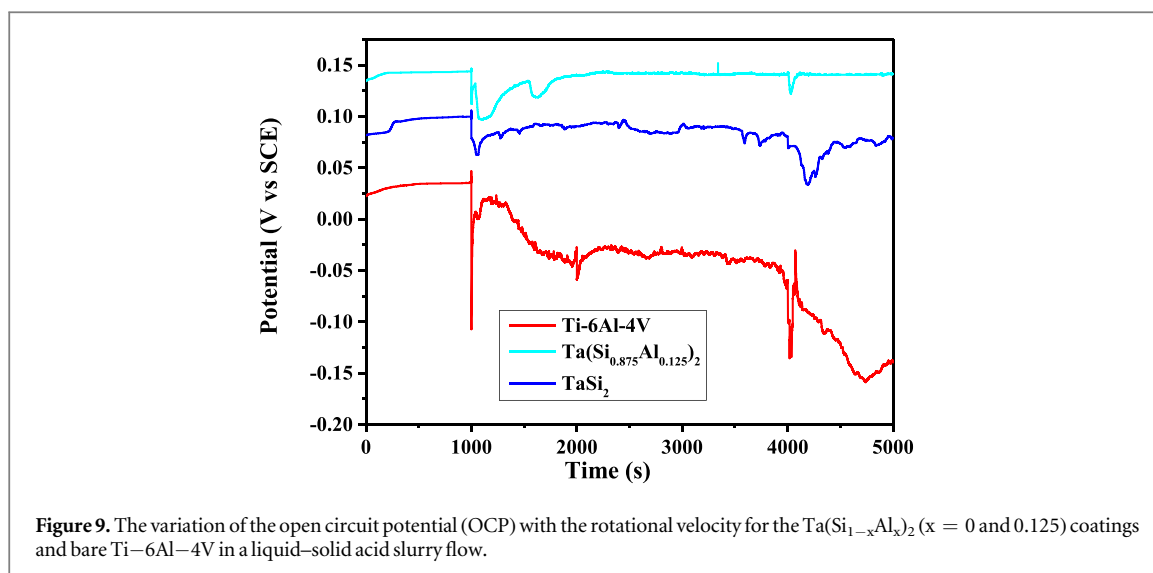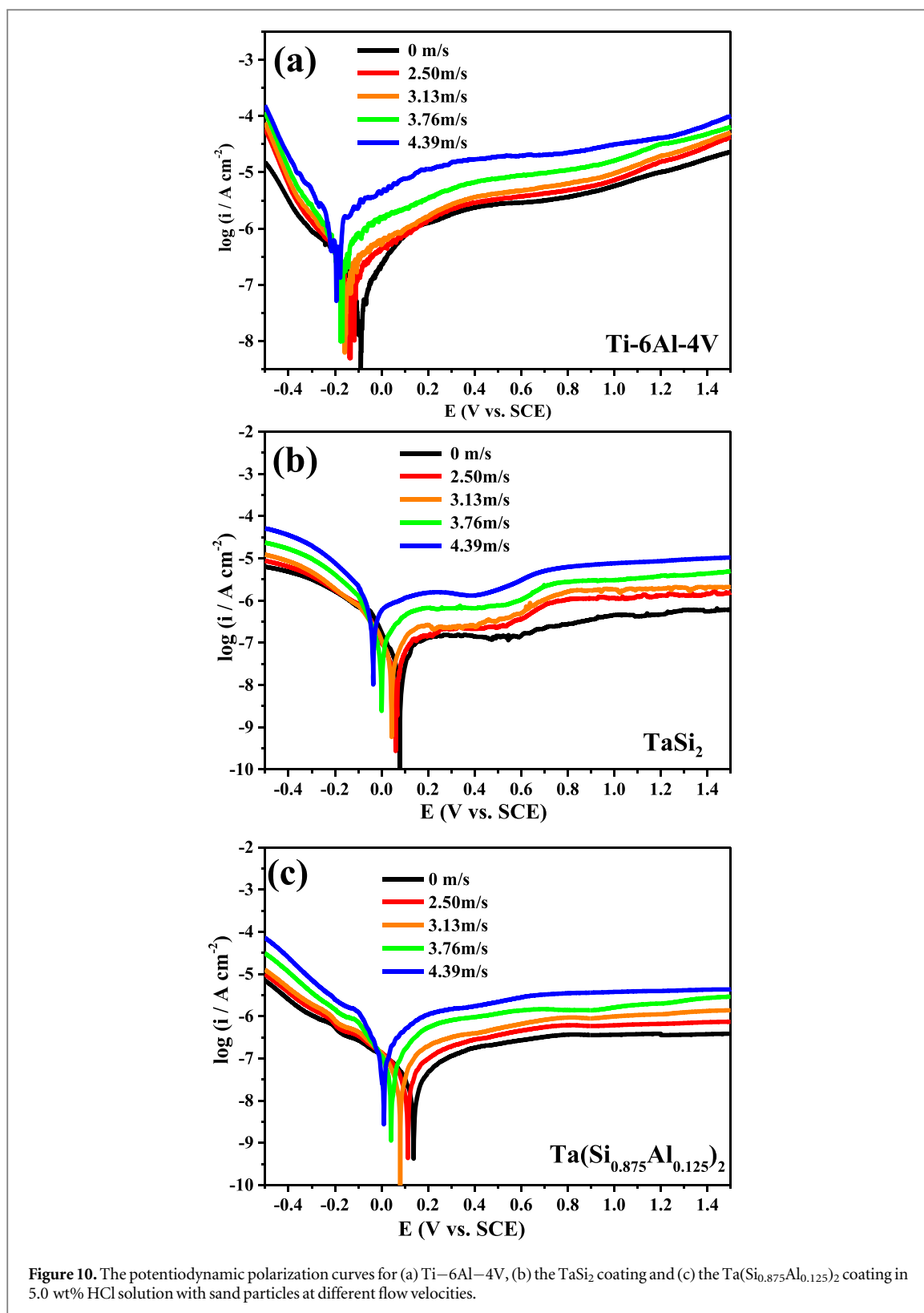
Figure 9. The variation of the open circuit potential (OCP) with the rotational velocity for the Ta(Si$_{1-x}$Al$_x$)$_2$ (x = 0 and 0.125) coatings and bare Ti−6Al−4V in a liquid–solid acid slurry flow.

Figure 9 shows the variation of the open circuit potential (OCP) with the rotational velocity for the Ta(Si$_{1-x}$Al$_x$)$_2$ (x = 0 and 0.125) coatings and bare Ti−6Al−4V in a liquid–solid acid slurry flow. It is clear that the OCP value for bare Ti−6Al−4V progressively decreases with increasing rotational velocity, and starts to decrease more noticeably when the rotational velocity reaches 4.39 m s^{-1}. This negative shift of OCP can be related to the removal of the protective oxide film caused by mechanical erosion effects, which not only make the Ti−6Al−4V surface more anodic but also lead to larger surface area exposed to the corrosive medium [30]. Conversely, the OCP values for the two coatings decreased slightly as the conditions transitioned from static to dynamic. For the binary TaSi$_2$ coating, as the rotational velocity increased, the OCP value declined but decreased more abruptly at a rotational velocity value of 4.39 m s^{-1}. However, the OCP value of the Ta(Si$_{0.875}$Al$_{0.125}$)$_2$ coating was almost independent of rotational velocity. Both coatings have more positive OCP values than bare Ti−6Al−4V, indicating that the two coatings are more stable in both thermodynamics and kinetics. As can be clearly seen, the Al addition shifts the OCP value of the TaSi$_2$ coating to a nobler potential, implying that Al alloying further improves the thermodynamic stability of the passive film grown on the binary TaSi$_2$ coating.

3.3.2. Potentiodynamic polarization curves
Figure 10 shows the potentiodynamic polarization curves for the Ta(Si$_{1-x}$Al$_x$)$_2$ (x = 0 and 0.125) coatings and bare substrate at rotational velocities of up to 4.39 m s^{-1} in an acid slurry flow. To compare the corrosion resistance of the coated and uncoated specimens, the corrosion potential (E$_{corr}$) and the corrosion current density (i_{corr}) are provided in table 1, where i_{corr} values were obtained by the Tafel extrapolation method [31]. Under either static or dynamic condition, all the polarization curves show typical passivation behavior, characterized by a wide passive plateau with very low currents recorded in the anodic branches up to the scanning terminating potential of +1.5 V$_{SCE}$. With increasing rotational velocity, both anodic and cathodic branches in all the polarization curves are extended gradually towards the region of higher current density and lower potential. For the hydrochloric acid medium used in this study, the main anodic and cathodic reactions are regulated by oxidation reaction and reduction of hydrogen ions and dissolved oxygen, respectively. An increase in rotational velocity accelerates the transportation of the corrosive species and dissolved oxygen to the sample surface, enhancing the cathodic reduction process. Meanwhile, the intensity of erosion-corrosion is a function of the energy of the eroded particles and the higher energy of impinging sand particles, the more severe will be the attack [32]. A higher rotational velocity endows the sand particles present in acid slurry flow with higher impact energy and increases the collision frequency between the sand particles and the tested specimens, thus leading to a higher current density to achieve a dynamic equilibrium between the formation rate and the dissolution rate of the passivation film. This signifies a higher corrosion tendency of the eroded surface, due to negative influence of the impacting sand particles on the chemical dissolution of the passive films formed on the tested specimens [33]. From table 1, it can be seen that with increasing rotational velocity, the E$_{corr}$ values become more active, similar to what are seen from the OCP versus time plots and the i_{corr} values get bigger. Before the potentiodynamic sweep, the specimen was polarized cathodically for 10 min at −0.8 V$_{SCE}$ to remove part of the oxide layer formed on the specimen surface [34]. Hence, the E$_{corr}$ values determined from the polarization curves are more negative than the OCP values. At an identical rotational velocity, the i_{corr} value of the Ta(Si$_{0.875}$Al$_{0.125}$)$_2$ coating is lowest, followed by the TaSi$_2$ coating; uncoated Ti−6Al−4V has the highest value. The E$_{corr}$ values of the tested samples are in the reverse order relative to the i_{corr} values. This suggests that

Figure 10. The potentiodynamic polarization curves for (a) Ti−6Al−4V, (b) the $TaSi_2$ coating and (c) the $Ta(Si_{0.875}Al_{0.125})_2$ coating in 5.0 wt% HCl solution with sand particles at different flow velocities.

the $Ta(Si_{0.875}Al_{0.125})_2$ coating has superior erosion-corrosion resistance to the other two samples in acid slurry flow.

3.3.3. Electrochemical impedance spectroscopy (EIS) measurements

For a better understanding of the associated deterioration process of the $Ta(Si_{1−x}Al_x)_2$ (x = 0 and 0.125) coatings in acidic slurry flow, detailed EIS studies were carried out on both coatings after 0, 24,72 and 120 h of exposure to acid slurry flow at a rotational velocity of 4.39 m s^{-1}, as shown in figure 11. Prior to the erosion-corrosion tests (under static conditions), both the coatings and bare substrate show a clear capacitive response,

Table 1. Polarization parameters of the Ta(Si$_{1-x}$Al$_x$)$_2$ (x = 0 and 0.125) coatings and uncoated Ti−6Al−4V under slurry impingement at various flow velocities.

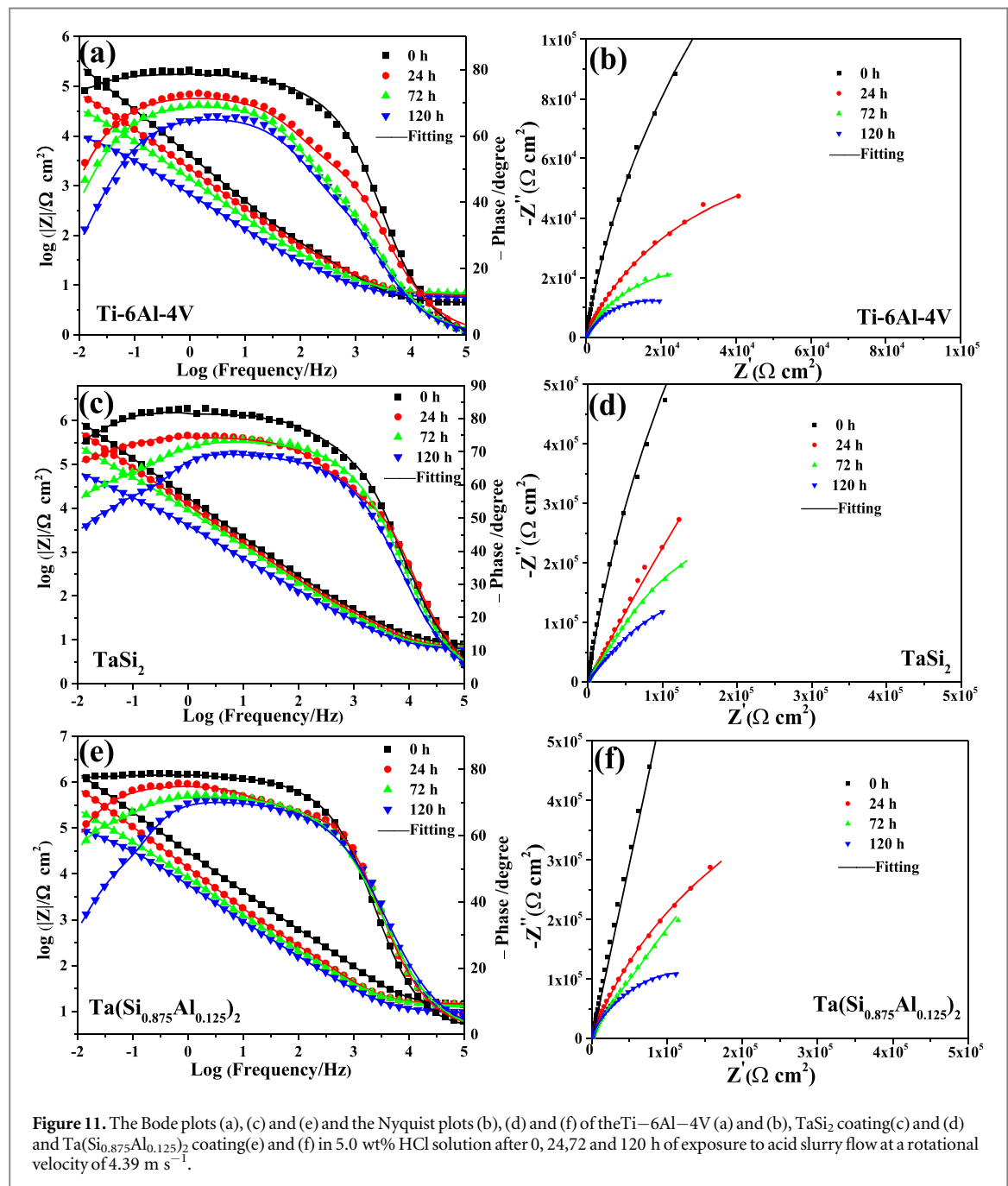|	TaSi$_2$		Ta(Si$_{0.875}$Al$_{0.125}$)$_2$		Ti−6Al−4V	
	E_{corr}(V$_{SCE}$)	i_{corr}(Acm^{-2})	E_{corr}(V$_{SCE}$)	i_{corr}(A cm^{-2})	E_{corr}(V$_{SCE}$)	i_{corr}(A cm^{-2})
0 m s^{-1}	0.078	3.98×10^{-8}	0.138	3.21×10^{-8}	−0.089	1.09×10^{-7}
2.50 m s^{-1}	0.060	6.44×10^{-8}	0.113	5.57×10^{-8}	−0.137	2.59×10^{-7}
3.13 m s^{-1}	0.043	8.98×10^{-8}	0.080	7.73×10^{-8}	−0.159	5.92×10^{-7}
3.76 m s^{-1}	0.002	1.43×10^{-7}	0.041	1.96×10^{-7}	−0.176	1.01×10^{-6}
4.39 m s^{-1}	−0.036	6.49×10^{-7}	0.003	3.24×10^{-7}	−0.199	2.81×10^{-6}

Figure 11. The Bode plots (a), (c) and (e) and the Nyquist plots (b), (d) and (f) of the Ti−6Al−4V (a) and (b), TaSi$_2$ coating (c) and (d) and Ta(Si$_{0.875}$Al$_{0.125}$)$_2$ coating (e) and (f) in 5.0 wt% HCl solution after 0, 24, 72 and 120 h of exposure to acid slurry flow at a rotational velocity of 4.39 m s^{-1}.

manifested by high impedance modulus |Z| at the low-frequency limit and the corresponding maximum phase angle close to −90° in the Bode plots, as well as with a larger diameter of non-compressed capacitive loop in Nyquist plots. The shape of these EIS plots is typical of the passive character observed during impedance spectroscopy of other passive metals or alloys [35]. The diameters of the capacitive loops represent the

Figure 12. Electronic equivalent circuit (EEC) used in the fitting procedure: (a) Ti−6Al−4V and the two coatings in static state; (b) Ti−6Al−4V and the two coatings after impingement.
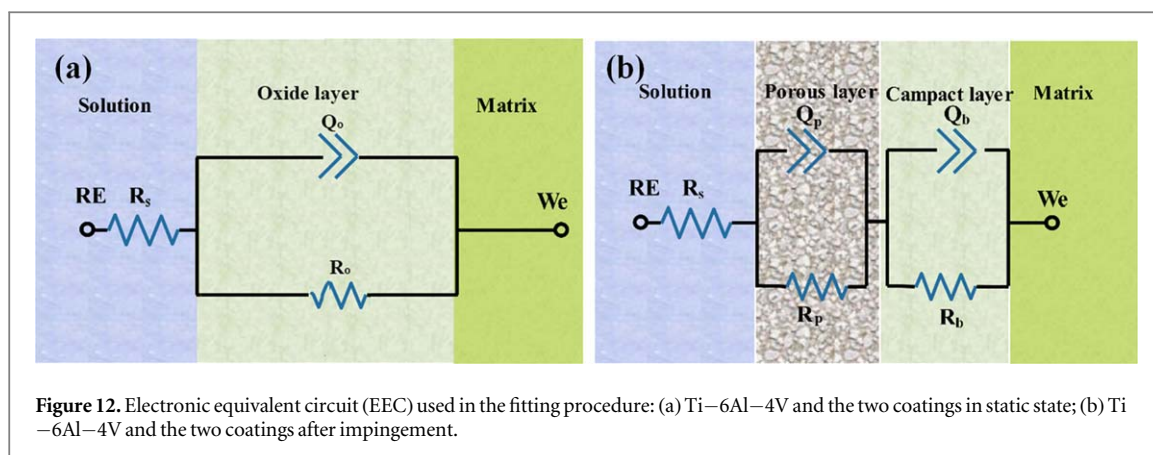
electrochemical reaction resistance, and larger diameters imply larger electrochemical reaction resistance and thus higher corrosion resistance [36]. According to the diameters of the capacitive arcs, the corrosion resistance of the tested specimens increases in the order of Ti−6Al−4V < TaSi$_2$ coating < Ta(Si$_{0.875}$Al$_{0.125}$)$_2$ coating under static condition. Nevertheless, under erosion-corrosion conditions, as the erosion time increased, a marked decrease in both the diameter of the capacitive arc in Nyquist plots and impedance modulus |Z| at the low-frequency limit in the Bode-magnitude plots are observed. Also, with increasing erosion time, the frequency range showing capacitive behavior becomes narrower and the maximum phase angle moves to higher frequencies in the Bode- phase angle plots. These results indicate that the protective properties of the passive layers which formed on the test specimens gradually decrease with increasing erosion exposure time. This arises from the ingress of corrosive medium into the passive films [37]. Compared to bare Ti−6Al−4V, the two Ta(Si$_{1-x}$Al$_x$)$_2$ coatings exhibit slower degradation with increasing erosion-corrosion time, indicating the improved corrosion protection afforded by the Ta(Si$_{1-x}$Al$_x$)$_2$ coatings.

To obtain quantitative analysis of the experimental impedance data, two different equivalent electron circuits are proposed to fit the collected impedance spectra for the tested samples shown in figure 12. The calculated elements from the proposed equivalent circuits are summarized in table 2. Some researchers [38, 39] have employed the equivalent circuit models with two time constants to determine the impedance parameters for titanium and coated systems exposed to acidic environments. In our case, it seems that the electrochemical behavior of both the Ta(Si$_{1-x}$Al$_x$)$_2$ coatings and bare Ti−6Al−4V is regulated by only a single time constant behavior under static conditions, because of large fitting errors for some of the circuit elements if an equivalent circuit model with two time constants is used. Hence, the impedance spectra collected from the tested samples in static 5 wt% HCl solution can be explained by a simple R$_s$–R$_o$Q$_o$ equivalent circuit (figure 12(a)), which is indicative of a single, thin passive oxide layer naturally grown on the surfaces of the samples. In this equivalent circuit model, Rs refers to the ohmic resistance of the electrolyte, the parameters R$_o$(passive film resistance) in parallel with the Q$_o$ (passive film capacitance) reflect the properties of the electrochemical reactions at the interface between the electrolyte and passive film. Owing to inhomogeneities in the passive film both on a microscopic and macroscopic scale, the capacitances were simulated by the frequency distributed element CPE (constant phase element) to get a better quality fit. The impedance of CPE (Z$_{CPE}$) is expressed as $Z_{CPE} = [Q(j\omega)^n]^{-1}$, where Q is a constant parameter (with dimensions Ω^{-1} cm^{-2} s^n), ω is the angular frequency (rad s^{-1}) defined as $\omega = 2\pi f$, j is the imaginary number and n is the meaning of the phase shift, which value reflects the surface inhomogeneity [40]. A CPE with a n value of 1 represents an ideal capacitor, where n = 0.5, the CPE represents a Warburg impedance, manifested by producing a 45° line on Nyquist plots. From inspection of the impedance spectra obtained from the tested samples after different erosion-corrosion times, the spectra reveal two relaxation processes with corresponding time constants, appearing in both the high and low frequency regions, respectively. Therefore, those impedance spectra are simulated by using an equivalent circuit composed of two RC circuits connected in series as: (R$_s$(Q$_p$R$_p$)(Q$_b$R$_b$)) (figure 12(b)), which relates to the formation of a bilayer structured passive film [41]. In this equivalent electric circuit, R$_p$ and Q$_p$ represent the resistive and capacitive behavior of an external porous layer with a higher frequency time constant, respectively; R$_b$ and Q$_b$ represent the resistive and capacitive behavior of an inner compact layer with a lower frequency time constant. As can be seen from the Bode plots, the experimental (individual points) and simulated (solid lines) data matched very well and the Chi square values (χ^2) are all on the order of 10^{-3}, indicative of a good fit with the proposed equivalent circuits. It can be seen from table 2 that the resistance in a static 5 wt% HCl solution is the highest for the Ta(Si$_{0.875}$Al$_{0.125}$)$_2$ coating, followed by the TaSi$_2$ coating and then bare alloy substrate. This observation is consistent with the outcomes from potentiodynamic polarization tests under static conditions.

Table 2. Electrochemical parameters obtained from numerical fitting for the $Ta(Si_{1-x}Al_x)_2$ (x = 0 and 0.125) coating and uncoated Ti−6Al−4V after different time of slurry impingement at the flow velocities of 4.39 s^{-1}.

0 h		R_s (Ω cm^2)	Q_o (Ω^{-1} cm^{-2}s^n)	n_o	$R_s(Q_oR_o)$ R_o (Ω cm^2)
	Ti−6Al−4V	5.84	1.09×10^{-5}	0.89	8.34×10^5
	TaSi$_2$	7.13	4.87×10^{-6}	0.90	4.96×10^6
	Ta(Si$_{0.875}$Al$_{0.125}$)$_2$	11.18	1.21×10^{-6}	0.93	5.27×10^6

24 h $\square$ $R_s(Q_pR_p)(Q_bR_b)$

	R_s (Ω cm^2)	Q_p (Ω^{-1} cm^{-2} s^n)	n_p	R_p (Ω cm^2)	Q_b (Ω^{-1} cm^{-2}s^n)	n_b	R_b (Ω cm^2)
Ti−6Al−4V	6.12	2.60×10^{-5}	0.8	65.28	1.37×10^{-5}	0.87	1.53×10^5
TaSi$_2$	6.53	9.46×10^{-6}	0.83	121.65	6.89×10^{-6}	0.89	8.73×10^5
Ta(Si$_{0.875}$Al$_{0.125}$)$_2$	11.88	7.62×10^{-6}	0.85	148.94	5.27×10^{-6}	0.91	9.56×10^5

72 h $\square$ $R_s(Q_pR_p)(Q_bR_b)$

	R_s (Ω cm^2)	Q_p (Ω^{-1} cm^{-2} s^n)	n_p	R_p (Ω cm^2)	Q_b (Ω^{-1} cm^{-2}s^n)	n_b	R_b (Ω cm^2)
Ti−6Al−4V	6.81	2.41×10^{-4}	0.77	53.96	1.79×10^{-5}	0.84	6.37×10^4
TaSi$_2$	6.59	3.72×10^{-5}	0.8	98.26	1.29×10^{-5}	0.87	5.53×10^5
Ta(Si$_{0.875}$Al$_{0.125}$)$_2$	10.48	2.69×10^{-5}	0.82	136.49	8.43×10^{-6}	0.88	6.78×10^5

120 h $\square$ $R_s(Q_pR_p)(Q_bR_b)$

	R_s (Ω cm^2)	Q_p (Ω^{-1} cm^{-2} s^n)	n_p	R_p (Ω cm^2)	Q_b (Ω^{-1} cm^{-2}s^n)	n_b	R_b (Ω cm^2)
Ti−6Al−4V	6.75	4.68×10^{-4}	0.74	44.37	1.84×10^{-4}	0.8	3.16×10^4
TaSi$_2$	9.22	6.93×10^{-5}	0.76	78.49	5.79×10^{-5}	0.82	1.51×10^5
Ta(Si$_{0.875}$Al$_{0.125}$)$_2$	9.62	4.47×10^{-5}	0.79	108.26	3.21×10^{-5}	0.84	2.57×10^5

After a range of exposure times to the acid slurry flow, the resistance of the external porous layer (R_p) is far less than that of the inner compact layer (R_b), because the highly defected external layer provides a penetrating path for aggressive species (including H$^+$ and Cl$^-$ ions) to penetrate the passive film [42]. Therefore, the overall corrosion protection of the passive films is highly dependent on the nature of the inner compact layer. With increasing slurry erosion-corrosion time, a decrease in resistance and an increase in capacitance were observed, indicating that the passive films formed on the test specimens have thinned and their conductivity is gradually enhanced. At a given erosion-corrosion time, the resistance of the compact layers (R_b values) are increased in order for the bare Ti−6Al−4V < TaSi$_2$ coating < Ta(Si$_{0.875}$Al$_{0.125}$)$_2$ coating. This demonstrates that bare Ti−6Al−4V is more susceptible to erosion-corrosion damage in acid slurry flow as compared to the two Ta(Si$_{1-x}$Al$_x$)$_2$ coatings and, moreover, Al addition can further improve the erosion-corrosion resistance of the TaSi$_2$ coating. As shown in table 2, bare Ti−6Al−4V has the lowest value for the parameter n for the CPE in the tested samples, implying that its surface exhibits larger open pores. Such a porous morphology is more likely to adsorb aggressive chloride ions and products soluble complex compounds such as TiOCl$_2$, giving rise to the occurrence of localized depassivation [43]. In contrast, the Al alloyed TaSi$_2$ coating exhibits the highest n value, indicating that the Al addition reduces the surface porosity of the passive film formed on the TaSi$_2$ coating. A more dense passive film more effectively retards the penetration of the electrolyte to the sample surface, which explains why the Ta(Si$_{0.875}$Al$_{0.125}$)$_2$ coating shows the higher charge transfer resistance as compared to the TaSi$_2$ coating or bare Ti−6Al−4V.

3.3.4. Weight loss measurements and eroded–corroded surface morphologies

As mentioned above, when specimens are exposed to liquid–solid impingement under the conditions of acid slurry flow, the synergism between corrosion and erosion includes two aspects: erosion-enhanced corrosion caused by impinging action of solid particles removing any protective film and corrosion-enhanced erosion induced by an corrosive attack lowering the mechanical properties of the surface layer [44]. To resolve the individual roles of corrosion and erosion interactions in the degradation of the tested samples in acid slurry flow, the synergistic weight loss (W_s) is computed by subtracting weight loss from pure erosion (W_e) and weight loss from pure corrosion (W_c) from the total weight loss (W_t), which can be expressed as:
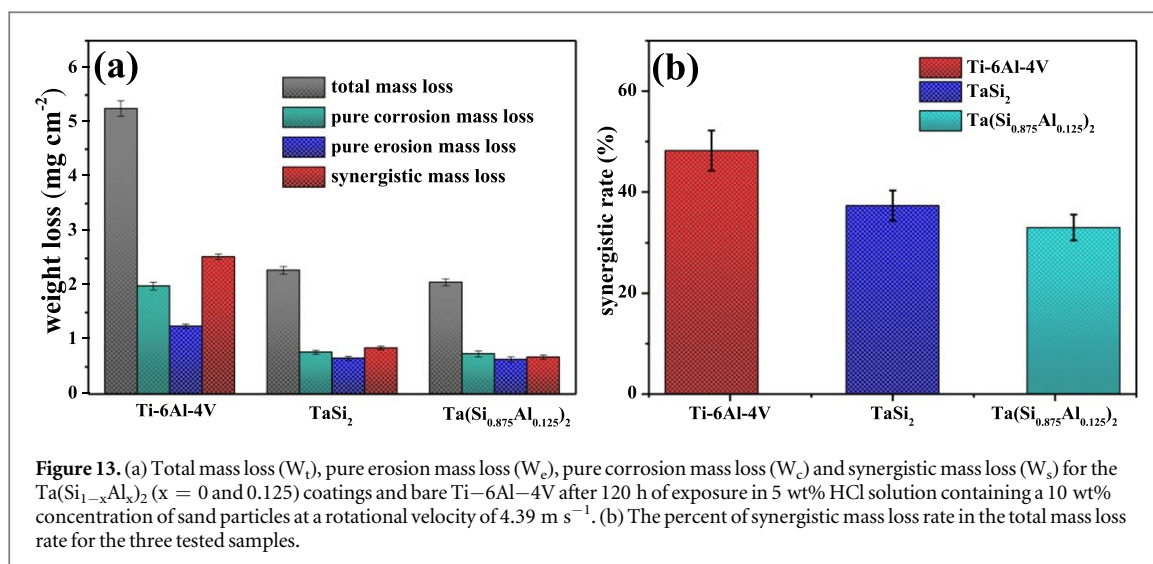
Figure 13. (a) Total mass loss (W_t), pure erosion mass loss (W_e), pure corrosion mass loss (W_c) and synergistic mass loss (W_s) for the Ta($Si_{1-x}Al_x$)$_2$ (x = 0 and 0.125) coatings and bare Ti−6Al−4V after 120 h of exposure in 5 wt% HCl solution containing a 10 wt% concentration of sand particles at a rotational velocity of 4.39 m s^{-1}. (b) The percent of synergistic mass loss rate in the total mass loss rate for the three tested samples.

$$W_t = W_e + W_c + W_s \qquad (1)$$

The total weight loss (W_t) and the independent contributing components (including weight loss of pure erosion (W_e), weight loss of pure corrosion (W_c) and synergistic weight loss (W_s)) for the Ta($Si_{1-x}Al_x$)$_2$ (x = 0 and 0.125) coatings and bare Ti−6Al−4V after 120 h of exposure in a 5 wt% HCl solution containing a 10 wt% concentration of silica sand particles at a rotational velocity of 4.39 m s^{-1} are shown in figure 13. From figure 13(a), one may see that whether the total weight loss (W_t), or the individual components (including W_c, W_e and W_s) for the uncoated substrate is distinctly greater than that for the two coatings for a given concentration of sand particles and rotational speed. For all the tested samples, the weight loss from pure corrosion (W_c) is larger than that from pure erosion (W_e), suggesting that pure corrosion plays a greater role in material removal than pure erosion in the case of the acid slurry flow used here. As shown in figure 13(a), the order of the proportion of W_s to W_t for the tested samples is as follows: Ti−6Al−4V > TaSi$_2$ coating > Ta($Si_{0.875}Al_{0.125}$)$_2$ coating. Distinct from the Ta($Si_{0.875}Al_{0.125}$)$_2$ coating, the synergistic weight losses (W_s) for the TaSi$_2$ coating and uncoated substrate account for the major contribution to the total weight loss (W_t). This indicates that their erosion-corrosion resistance is predominantly determined by synergism-induced weight loss. In general, the differences in the resistance to slurry erosion-corrosion for the three tested samples correlate with both their mechanical properties and electrochemical performance. From the perspective of the mechanical erosion properties of a material, the severity of the pure erosion rate depends upon the ratio of the hardness of the sand particles (∼750 HV for quartz/silica) to that of the hardness of the eroded surface of tested samples [45]. The greater the hardness of a material, the lower the pure erosion rate. Compared to bare Ti−6Al−4V, the two silicide coatings show lower ratios and thus exhibit a larger ability to withstand the abrading action of the sand particles [46]. Hence, the two coatings exhibit lower weight loss of pure erosion than bare Ti−6Al−4V. Ji *et al* [47] evaluated the erosive wear behavior of an aluminum alloy, titanium alloys and AlCrFeCoNiCu high-entropy alloy in slurry flow composed of water and 1 wt% SiO$_2$ particles. They found that there was a significant positive linear relationship between the slurry erosive wear resistance and H/E ratio. As noted in figures 6(b) and 7, although Al alloying reduces slightly the hardness of the TaSi$_2$ coating, the Ta($Si_{0.875}Al_{0.125}$)$_2$ coating exhibits higher H/E ratio and adhesion strength between the coating and Ti−6Al−4V substrate, which may explain the lower material removal rate under the action of impacting particles.

In terms of corrosion, the Ta($Si_{0.875}Al_{0.125}$)$_2$ coating shows the highest corrosion resistance in the tested samples under both static and dynamic conditions. Unlike static corrosion condition, the suspended solid particles in acid solution exert a shearing stress upon the sample surface, destroying the integrity of its surface passive film and thus exposing the underlying substrate to the slurry medium. This accelerates anodic dissolution of the surface deformed region and hence results in a higher current density. The electrochemical corrosion, in turn, would thus weaken the mechanical properties of sample surface, leading to a reduction of resistance against sand impingement. As observed in figures 8 and 10, compared with the TaSi$_2$ coating and uncoated Ti−6Al−4V, the Ta($Si_{0.875}Al_{0.125}$)$_2$ coating possesses a higher self-healing ability for the passive film once damage occurs. In our previous study[], the chemical composition of the passive films grown on the binary β-Ta$_5$Si$_3$ coating and the ternary β-Ta$_5$($Si_{0.83}Al_{0.17}$)$_3$ coating in 3.5 wt% NaCl solution was investigated using XPS measurements. The results indicated that the passive film formed on the β-Ta$_5$($Si_{0.83}Al_{0.17}$)$_3$ coating exhibits higher SiO$_2$ concentrations than that for the binary β-Ta$_5$Si$_3$ coating. The increased SiO$_2$ concentration for the ternary coating may be linked to the change of the chemical bond strengths of β-Ta$_5$Si$_3$ by Al addition.
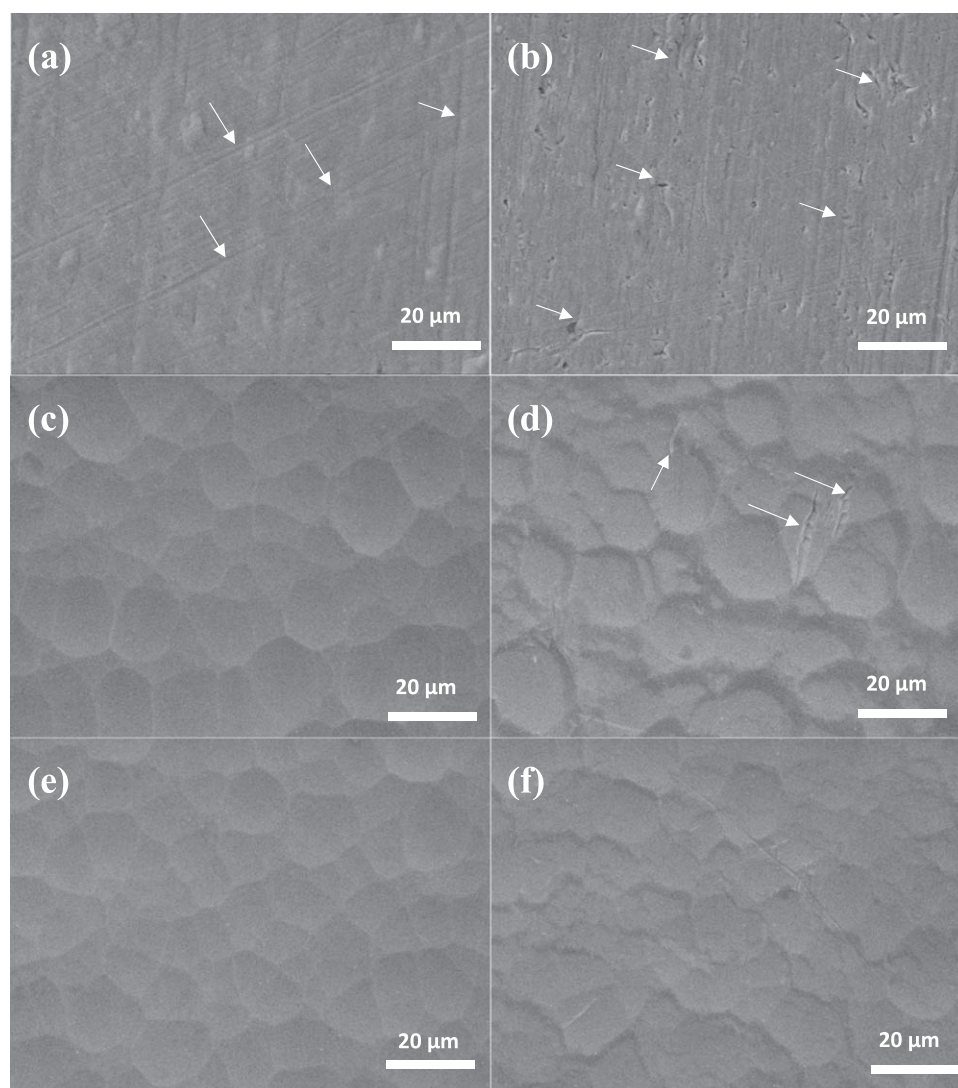
Figure 14. Surface morphologies of damaged surfaces for (a) and (b) the bare Ti−6Al−4V, (c) and (d) the TaSi$_2$ coating, (e) and (f) the Ta(Si$_{0.875}$Al$_{0.125}$)$_2$ coating after (a), (c) and (e) 0 h and (b), (d) and (f) 120 h exposure to liquid–solid two phase slurry flow at flow velocity of 4.39 m s^{-1}.

Because SiO$_2$ has higher dielectric characteristics and a lower oxygen diffusion coefficient as compared to Ta$_2$O$_5$, the β-Ta$_5$(Si$_{0.83}$Al$_{0.17}$)$_3$ coating, with a higher content concentration of SiO$_2$, provides its passive film with a higher corrosion resistance in comparison to the binary β-Ta$_5$Si$_3$ coating. In the present study, it is safe assumption that similar phenomenon maybe take place on the Ta(Si$_{1-x}$Al$_x$)$_2$ nanocrystalline coatings, because both β-Ta$_5$Si$_3$ and TaSi$_2$ belong to Ta silicides. Therefore, the Ta(Si$_{0.875}$Al$_{0.125}$)$_2$ coating provides better protection against the combined attack of mechanical erosion and electrochemical corrosion in a liquid–solid acid slurry flow.

Figure 14 shows a comparison of eroded-corroded surfaces for the Ta(Si$_{1-x}$Al$_x$)$_2$ (x = 0 and 0.125) coatings and bare Ti−6Al−4V both before and after 120 h of exposure to a 5 wt% HCl solution containing a 10 wt% concentration of sand particles at a rotational velocity of 4.39 m s^{-1}. It can be seen from figures 14(a) and (b) that some small craters and ploughed grooves are present on the eroded-corroded surface of the bare alloy substrate, in addition to presence of pre-existing polishing marks. These damage characteristics result from the penetration and scratching of the sand particles on the eroded-corroded surface. As shown in figures 14(c) and (d), the surface of the TaSi$_2$ coating exhibits lesser surface damage than bare alloy, evidenced by a few ploughed grooves and shallow denudation due to its relatively high brittleness. As shown in figures 14(e) and (f), much of the Ta(Si$_{0.875}$Al$_{0.125}$)$_2$ original as-deposited coating is retained, indicating that the Al addition improves the erosion-corrosion resistance of the TaSi$_2$ coating in a liquid–solid acid slurry flow. The results of these erosion–corrosion observations of the exposed surfaces are also in accordance with the observed current response, potentiodynamic polarization and EIS curves.

4. Conclusions

To determine the effects of Al addition on the erosion–corrosion resistance of a $TaSi_2$ coating, both binary $TaSi_2$ and ternary $Ta(Si_{0.875}Al_{0.125})_2$ coatings were prepared onto Ti—6Al—4V substrates using the double cathode glow discharge method. The two $Ta(Si_{1-x}Al_x)_2$ coatings with a thickness of ~15 μm exhibit a dense and homogenous structure. The silicide coatings are comprised of fine (~5 nm diameter) equiaxed grains. Al addition lower the hardness and Young's modulus for $TaSi_2$, but increase the values of H/E, H^3/E^2 and $1/HE^2$. Scratch testing suggest that the $Ta(Si_{0.875}Al_{0.125})_2$ coating has a higher adhesion strength and crack initiation load than the $TaSi_2$ coating. The potentiodynamic polarisation tests indicated that with increasing rotational velocity, the E_{corr} values became more active and i_{corr} values decrease. At an identical rotational velocity, the $Ta(Si_{0.875}Al_{0.125})_2$ coating exhibited the lowest i_{corr} value and highest E_{corr} value amongst the tested samples. EIS measurements showed that with increasing slurry erosion-corrosion time, the resistance values of the tested samples decreased, and for a given erosion-corrosion time, the resistances value are increased by the order of bare Ti—6Al—4V < $TaSi_2$ coating < $Ta(Si_{0.875}Al_{0.125})_2$ coating. The excellent erosion-corrosion properties of the ternary coating can be related to its high H/E value as well as the higher self-healing ability of its surface passive film.

Acknowledgments

ORCID iDs

Jiang Xu ⓘ https://orcid.org/0000-0002-0925-9591

References

[1] Zhao W, Wang Y, Liu C, Dong L, Yu H and Ai H 2010 Erosion–corrosion of thermally sprayed coatings in simulated splash zone *Surf. Coat. Technol.* **205** 2267–72

[2] Wood R J K 2006 Erosion-corrosion interactions and their effect on marine and offshore materials *Wear* **261** 1012–23

[3] Finnie I 1995 Some reflections on the past and future of erosion *Wear* **186** 1–10

[4] Purandare Y P, Stack M M and Hovsepian P E 2006 Velocity effects on erosion–corrosion of CrN/NbN 'superlattice' PVD coatings *Surf. Coat. Technol.* **201** 361–70

[5] Pagalthivarthi K V, Gupta P, Tyagi V and Ravi M R 2011 CFD prediction of erosion wear in centrifugal slurry pumps for dilute slurry flows *The Journal of Computational Multiphase Flows* **3** 225–46

[6] Bozzini B, Ricotti M E, Boniardi M and Mele C 2003 Evaluation of erosion–corrosion in multiphase flow via CFD and experimental analysis *Wear* **255** 237–45

[7] Wang Z B, Zheng Y G and Yi J Z 2019 The role of surface film on the critical flow velocity for erosion-corrosion of pure titanium *Tribol. Int.* **133** 67–72

[8] Aribo S, Fakorede A, Ige O and Olubambi P 2017 Erosion-corrosion behaviour of aluminum alloy 6063 hybrid composite *Wear* **376-377** 608–14

[9] Bermúdez M D, Carrión F J, Martínez Nicolás G and López R 2005 Erosion–corrosion of stainless steels, titanium, tantalum and zirconium *Wear* **258** 693–700

[10] Chen J, Zhang Q, Li Q, Fu S and Wang J 2014 Corrosion and tribocorrosion behaviors of AISI 316 stainless steel and Ti6Al4V alloys in artificial seawater *Transactions of Nonferrous Metals Society of China* **24** 1022–31

[11] Niu Y, Huang L, Zhai C, Zeng Y, Zheng X and Ding C 2015 Microstructure and thermal stability of $TaSi_2$ coating fabricated by vacuum plasma spray *Surf. Coat. Technol.* **279** 1–8

[12] Maglia F, Milanese C, Anselmi-Tamburini U, Doppiu S, Cocco G and Munir Z A 2004 Combustion synthesis of mechanically activated powders in the Ta–Si system *J. Alloys Compd.* **385** 269–75

[13] Xu J, Liu W, Jiang S Y, Munroe P and Xie Z H 2019 Enhancing the cavitation erosion resistance of $D8_{(m)}$-Ta_5Si_3 nanocrystalline coatings through Al alloying *Ultrason. Sonochem.* **50** 138–56

[14] Oliver W C and Pharr G M 1992 An Improved Technique for determining hardness and elastic modulus using load and displacement sensing indentation experiments *J. Mater. Res.* **7** 1564–83

[15] Xu J, Zhuo C, Han D, Tao J, Liu L and Jiang S 2009 Erosion–corrosion behavior of nano-particle-reinforced Ni matrix composite alloying layer by duplex surface treatment in aqueous slurry environment *Corros. Sci.* **51** 1055–68

[16] Paul A, Kodentsov A A, de With G and van Loo F J J 2003 Formation of AB_2-intermetallics by diffusion in the Au–Sb–Bi system *Intermetallics* **11** 1195–203

[17] Carvalho S, Ribeiro E, Rebouta L, Vaz F, Alves E, Schneider D and Cavaleiro A 2003 Effects of the morphology and structure on the elastic behavior of (Ti,Si,Al)N nanocomposites *Surf. Coat. Technol.* **174-175** 984–91

[18] Liu C, Bi Q, Leyland A and Matthews A 2003 An electrochemical impedance spectroscopy study of the corrosion behaviour of PVD coated steels in 0.5 N NaCl aqueous solution: Part II. EIS interpretation of corrosion behaviour *Corros. Sci.* **45** 1257–73

[19] Shon I J, Ko I Y, Chae S M and Na K.i. 2011 Rapid consolidation of nanostructured $TaSi_2$ from mechanochemically synthesized powder by high frequency induction heated sintering *Ceram. Int.* **37** 679–82

[20] Cui C, Zhang J, Liu L and Fu H 2010 Mechanical Properties of the TaSi$_2$ Fibers by Nanoindentation *J. Mater. Sci. Technol.* **26** 65–8

[21] Xu J, Cheng J, Jiang S, Munroe P and Xie Z 2017 The influence of Ti additions on the mechanical and electrochemical behavior of β-Ta$_5$Si$_3$ nanocrystalline coating *Appl. Surf. Sci.* **419** 901–15

[22] Leyland A and Matthews A 2000 On the significance of the H/E ratio in wear control: a nanocomposite coating approach to optimised tribological behaviour *Wear* **246** 1–11

[23] Musil J 2012 Hard nanocomposite coatings: thermal stability, oxidation resistance and toughness *Surf. Coat. Technol.* **207** 50–65

[24] Abd El-Rahman A M and Wei R H 2014 Effect of ion bombardment on structural, mechanical, erosion and corrosion properties of Ti–Si–C–N nanocomposite coatings *Surf. Coat. Technol.* **258** 320–8

[25] Weaver J C *et al* 2010 Analysis of an ultra hard magnetic biomineral in chiton radular teeth *Mater. Today* **13** 42–52

[26] Kabir M S, Munroe P, Gonçales V, Zhou Z and Xie Z 2018 Structure and properties of hydrophobic CeO$_{2-x}$ coatings synthesized by reactive magnetron sputtering for biomedical applications *Surf. Coat. Technol.* **349** 667–76

[27] Kabir M S, Munroe P, Zhou Z and Xie Z 2017 Scratch adhesion and tribological behaviour of graded Cr/CrN/CrTiN coatings synthesized by closed-field unbalanced magnetron sputtering *Wear* **380-381** 163–75

[28] Burstein G T and Sasaki K 2000 The birth of corrosion pits as stimulated by slurry erosion *Corros. Sci.* **42** 841–60

[29] Burstein G T, Liu C, Souto R and Vines S 2004 Origins of pitting corrosion *Corrosion Engineering Science and Technology* **39** 25–30

[30] Wang X Y and Li D Y 2005 Application of an electrochemical scratch technique to evaluate contributions of mechanical and electrochemical attacks to corrosive wear of materials *Wear* **259** 1490–6

[31] Koike M, Cai Z, Fujii H, Brezner M and Okabe T 2003 Corrosion behavior of cast titanium with reduced surface reaction layer made by a face-coating method *Biomaterials* **24** 4541–9

[32] Das S, Saraswathi Y L and Mondal D P 2006 Erosive–corrosive wear of aluminum alloy composites: influence of slurry composition and speed *Wear* **261** 180–90

[33] Hu P, Song R, Deng J, Chen Z Y, Li Q W, Hu B L, Wang K S, Cao W C, Liu D X and Yu H L 2017 Electrochemical corrosion behavior of platinum-coated lanthanum doped titanium-zirconium-molybdenum alloy *J. Alloys Compd.* **706** 305–11

[34] Luiz de Assis S, Wolynec S and Costa I 2006 Corrosion characterization of titanium alloys by electrochemical techniques *Electrochim. Acta* **51** 1815–9

[35] Valero Vidal C and Igual Muñoz A 2010 Study of the adsorption process of bovine serum albumin on passivated surfaces of CoCrMo biomedical alloy *Electrochim. Acta* **55** 8445–52

[36] Lv J, Liang T and Chen W 2016 Surface enriched molybdenum enhancing the corrosion resistance of 316L stainless steel *Mater. Lett.* **171** 38–41

[37] Liu X, Xiong J, Lv Y and Zuo Y 2009 Study on corrosion electrochemical behavior of several different coating systems by EIS *Prog. Org. Coat.* **64** 497–503

[38] Badawy W, Elegamy S S and Ismail K 1993 Comparative study of tantalum and titanium passive films by electrochemical impedance spectroscopy *Br. Corros. J.* **28** 133–6

[39] Grips V K W, Ezhil Selvi V, Barshilia H C and Rajam K S 2006 Effect of electroless nickel interlayer on the electrochemical behavior of single layer CrN, TiN, TiAlN coatings and nanolayered TiAlN/CrN multilayer coatings prepared by reactive dc magnetron sputtering *Electrochim. Acta* **51** 3461–8

[40] Wang D, Liu Y, Hu H, Zeng Z, Zhou F and Liu W 2008 Electrochemical Characterization of the Solution Accessibility of CaTiO$_3$ Microstructures and Improved Biomineralization *J. Phys. Chem.* C **112** 16123–9

[41] Zhou X and Mohanty P 2012 Electrochemical behavior of cold sprayed hydroxyapatite/titanium composite in Hanks' solution *Electrochim. Acta* **65** 134–40

[42] Li D G, Wang J D and Chen D R 2012 Influence of ytterbium on the electrochemical property of PbCaSn alloy in sulfuric acid solution *J. Power Sources* **210** 163–71

[43] Shokouhfar M, Dehghanian C, Montazeri M and Baradaran A 2012 Preparation of ceramic coating on Ti substrate by plasma electrolytic oxidation in different electrolytes and evaluation of its corrosion resistance: II *Appl. Surf. Sci.* **258** 2416–23

[44] Stack M M and Badia T M A E 2006 Mapping erosion–corrosion of WC/Co–Cr based composite coatings: Particle velocity and applied potential effects *Surf. Coat. Technol.* **201** 1335–47

[45] Clark H M and Llewellyn R J 2001 Assessment of the erosion resistance of steels used for slurry handling and transport in mineral processing applications *Wear* **250** 32–44

[46] Luiset B, Sanchette F, Billard A and Schuster D 2013 Mechanisms of stainless steels erosion by water droplets *Wear* **303** 459–64

[47] Ji X L, Ji C C, Cheng J B, Shan Y P and Tian S Y 2018 Erosive wear resistance evaluation with the hardness after strain-hardening and its application for a high-entropy alloy *Wear* **398** 178–82